energies

Article

Adaptive Hybrid Fuzzy-Proportional Plus Crisp-Integral Current Control Algorithm for Shunt Active Power Filter Operation

Nor Farahaida Abdul Rahman [1,*], Mohd Amran Mohd Radzi [2], Azura Che Soh [2], Norman Mariun [2] and Nasrudin Abd Rahim [3]

1. Faculty of Electrical Engineering, Engineering Complex, Universiti Teknologi MARA, Shah Alam, Selangor 40450, Malaysia
2. Department of Electrical and Electronic Engineering, Faculty of Engineering, Universiti Putra Malaysia, Serdang, Selangor 43400, Malaysia; amranmr@upm.edu.my (M.A.M.R.); azuracs@upm.edu.my (A.C.S.); norman@upm.edu.my (N.M.)
3. UM Power Energy Dedicated Advanced Centre (UMPEDAC), University of Malaya, Kuala Lumpur 50603, Malaysia; nasrudin@um.edu.my

* Correspondence: farahaida@salam.uitm.edu.my; Tel.: +60-17-6723486

Academic Editor: Akhtar Kalam
Received: 21 July 2016; Accepted: 2 September 2016; Published: 13 September 2016

Abstract: An adaptive hybrid fuzzy-proportional plus crisp-integral current control algorithm (CCA) for regulating supply current and enhancing the operation of a shunt active power filter (SAPF) is presented. It introduces a unique integration of fuzzy-proportional (Fuzzy-P) and crisp-integral (Crisp-I) current controllers. The Fuzzy-P current controller is developed to perform gain tuning procedure and proportional control action. This controller inherits the simplest configuration; it is constructed using a single-input single-output fuzzy rule configuration. Thus, an execution of few fuzzy rules is sufficient for the controller's operation. Furthermore, the fuzzy rule is developed using the relationship of currents only. Hence, it simplifies the controller development. Meanwhile, the Crisp-I current controller is developed to perform integral control action using a controllable gain value; to improve the steady-state control mechanism. The gain value is modified and controlled using the Fuzzy-P current controller's output variable. Therefore, the gain value will continuously be adjusted at every sample period (or throughout the SAPF operation). The effectiveness of the proposed CCA in regulating supply current is validated in both simulation and experimental work. All results have proven that the SAPF using the proposed CCA is capable to regulate supply current during steady-state and dynamic-state operations. At the same time, the SAPF is able to enhance its operation in compensating harmonic currents and reactive power. Furthermore, the implementation of the proposed CCA has resulted more stable dc-link voltage waveform.

Keywords: shunt active power filter; harmonic and reactive power compensation; current control algorithm

1. Introduction

One of the common power quality problems in electrical power systems is the existence of harmonic currents. This problem is originated from nonlinear loads (NLs); they need to draw harmonic currents for their operation. Consequently, various undesirable phenomena such as transmission power losses, overheating of power factor (PF) capacitors, interference in communication lines, and malfunction of sensitive equipment have occurred. In order to compensate multiple harmonic currents simultaneously, shunt active power filters (SAPFs) are employed [1,2].

In general, SAPFs are utilized for compensating harmonic components of distorted supply currents. Also, they can be used to compensate reactive power for PF correction. These two functions can be achieved by injecting specific compensation currents into power systems. Subsequently, the shape of the supply currents becomes sinusoidal; it only consists of fundamental component and in phase with supply voltage (as PF is corrected). Normally, SAPFs are installed at the point of common coupling (PCC) near the end-user sides or NLs [3,4].

One of the most important algorithms in a SAPF operation is a current control algorithm (CCA). Basically, it is designed to regulate either compensation current or supply current using a direct or indirect current control strategy. Consequently, the controlled current can be tracked to follow the nature of its reference current; by controlling the SAPF's switching activity. The effectiveness of any CCA depends on the implementation of current controller and modulation technique. Various types of CCAs have been demonstrated. They are hysteresis [5–7], repetitive [8–10], predictive [11–13], sliding mode [14,15], and conventional or crisp-proportional-integral (Crisp-PI) [16–18] CCAs.

Owing to their simple implementation, fast response, high stability and good dynamic response, hysteresis controllers have been used widely in the operation of SAPFs [19–21]. However, they have one major drawback which is the generation of asymmetrical switching frequencies [22]. In order to obtain a symmetrical switching frequency, repetitive, predictive, sliding mode and Crisp-PI current controllers are employed. All these controllers are developed using mathematical models [23,24]. Nevertheless, Crisp-PI current controllers exhibit simpler mathematical model than the above-mentioned controllers [25].

Principally, the operation of a Crisp-PI controller involves two types of control mechanisms. First, a proportional control action for minimizing the steady-state error of a controlled variable; and second, an integral control action for eliminating the steady-state error. Both control mechanisms apply two different control gains namely as the proportional control gain K_p and the integral control gain K_i. However, since this controller implements fixed gain values, therefore, it inherits unsatisfactory performance in controlling nonlinear or time-varying systems such as SAPFs [26]. Furthermore, it takes a considerable time for the gain tuning procedure [27], and it is not worthwhile to allocate such a long time, just to obtain fixed gain values.

In later work, improvement has been made by introducing various methods to modify K_p and/ or K_i values in certain range during operation [19,24,28]. One of the methods is a fuzzy-proportional-integral (Fuzzy-PI) controller. However, this controller is rarely utilized in the operation of SAPFs; specifically, in the CCA. Until now, there is only a single work about the development of such controller [28].

A Fuzzy-PI current controller of a SAPF has been presented in [28]. It is constructed using a multiple-input single-output (MISO) fuzzy rule configuration. It is used to tune both K_p and K_i values by directly generating a switching pattern. However, in order to achieve precise control mechanism, this controller must execute very large fuzzy rules (49 rules). Hence, it complicates the hardware development. In addition, the development of the fuzzy rules becomes difficult because they are constructed using the SAPF's internal losses model. Eventually, during the practical implementation, this controller is unable to maintain good steady-state control performance. Nevertheless, although this controller still exhibits limited exploration, a potential of better implementation can be seen; by a possibility of the controller's structural improvement.

Therefore, this work presents significant improvement by uniquely integrating Fuzzy-P and crisp-integral (Crisp-I) current controllers. The fuzzy-P current controller is constructed using a single-input single-output (SISO) fuzzy rule configuration, for allowing less fuzzy rules implementation. It is developed for adaptively tuning both K_p and K_i values, and performing the proportional control action. Furthermore, its fuzzy rules are constructed using the relationship of currents only; it is simpler than using the internal losses model introduced in [28]. Then, a Crisp-I current controller as to perform the integral control action is integrated with the Fuzzy-P current controller. A controllable gain value is introduced in the operation of the Crisp-I current controller, for enhancing the steady-state control mechanism. Therefore, by considering adaptive capability together with hybrid (fuzzy and crisp) approach, the proposed integration is named as an adaptive hybrid Fuzzy-P plus Crisp-I (HFP+CI) current controller. The proposed hybrid controller is applied in a CCA based indirect control strategy. The effectiveness of the proposed controller in improving the steady-state control mechanism is studied, in both simulation and experimental work. It is based on the capability of a SAPF to regulate supply current and compensate harmonic currents and reactive power. Moreover, in simulation work, a comparison of the performance of the proposed CCA with Fuzzy-PI [28] and Crisp-PI [17] CCAs is also conducted.

This paper is organized in six sections. Section 2 explains the principle operation of a SAPF, and its control system. Section 3 discusses the development of the proposed CCA. Sections 4 and 5 deliberate simulation and experimental results. Lastly, Section 6 lists out conclusions about the performance and contributions of the work.

2. Principle Operation of Shunt Active Power Filter

Figure 1 describes the principle operation of a SAPF using a voltage source inverter (VSI) topology.

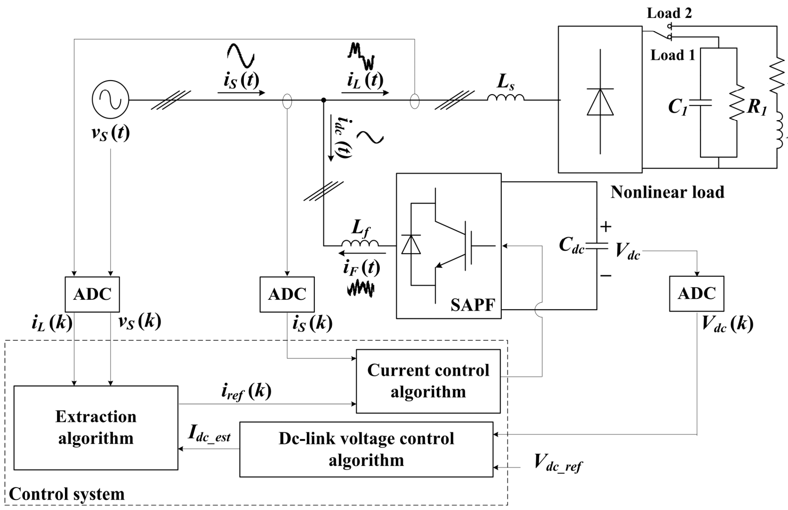

Figure 1. Control strategy for the operation of a SAPF.

According to the figure, the SAPF must inject the instantaneous compensation current $i_F(t)$ to the power system, for harmonic current and reactive power compensation. Besides injecting current, the SAPF is required to draw ac current (or active power) from the power system, for regulating dc-link voltage and compensating power loss. The ac current is known as the instantaneous dc-link charging current $i_{dc}(t)$. Consequently, the shape of the instantaneous supply current $i_S(t)$ waveform will be sinusoidal and in phase with the instantaneous supply voltage $v_S(t)$. At the same time, the shape of the instantaneous load current $i_L(t)$ remains unchanged. All the instantaneous currents can be represented as:

$$i_S(t) = i_L(t) - i_F(t) + i_{dc} = [i_{Fund}(t) + i_H(t)] - i_F(t) + i_{dc}(t) \quad (1)$$

where $i_{Fund}(t)$ is the instantaneous fundamental load current, and $i_H(t)$ is the instantaneous harmonic load currents. If $i_F(t)$ equals to $i_H(t)$, then the anticipated instantaneous compensated supply current $i_{S,comp}(t)$ can be represented as:

$$i_{S,comp}(t) = i_{Fund}(t) + i_{dc}(t) \quad (2)$$

According to Equation (2), it can be described that the supply current after the SAPF implementation must able to supply $i_{Fund}(t)$ for the operation of the NL, and $i_{dc}(t)$ for the regulation of the SAPF's dc-link voltage.

The operation of the SAPF depends fully on its control system. It consists of extraction algorithm, CCA and dc-link voltage control algorithm (VCA). These algorithms are normally executed using digital approach, and their operations are related to each other. The extraction algorithm is used to generate the digital time-varying reference current signal $i_{ref}(k)$, for the CCA. Note that k is the sampling data. In this work, unified adaptive linear neurons (ADALINEs)-based fundamental component extraction algorithms are used to generate $i_{ref}(k)$. Detailed explanation about the extraction algorithm can be found in [29]. On the other hand, a Crisp-PI dc-link VCA is utilized to regulate the dc-link voltage V_{dc}, by generating the estimated digital dc-link charging current signal $i_{dc,est}(k)$ [30]. All related parameters are converted to digital signals using analogue-to-digital converters (ADCs).

3. Proposed Adaptive Hybrid Fuzzy-Proportional Plus Crisp-Integral Current Control Algorithm

As mentioned, the proposed CCA is constructed using the indirect current control strategy and the proportional-integral control action. Instead of directly regulating $i_F(t)$, this CCA involves in regulating $i_S(t)$. Thus, $i_F(t)$ can indirectly be controlled. Moreover, in this work, the number of voltage and current sensors for 3-phase measurement is decreased from three to two sensors. The sensors are installed for measuring the voltage and current of phase a (phase angle 0°) and phase c (phase angle −240°) only. Hence, based on this measurement approach, the SAPF only needs to apply two separate current controllers for phase a and c, respectively. A block diagram of the proposed CCA for 3-phase operation is shown in Figure 2.

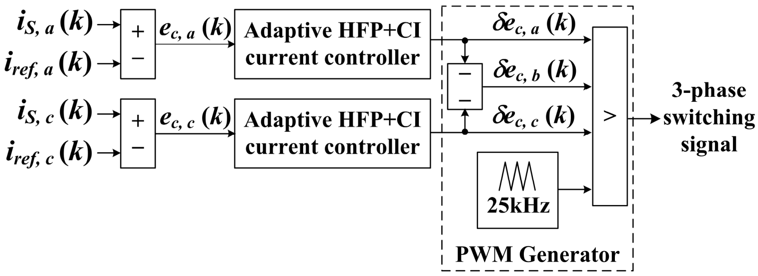

Figure 2. Proposed CCA for 3-phase operation.

As shown in the figure, the proposed CCA only consists of two proposed hybrid controllers together with a pulse width modulation (PWM) generator. According to the figure, the operation of the proposed CCA starts by obtaining the digital time-varying current error signal $e_{c,ix}(k)$:

$$e_{c,ix}(k) = i_{S,ix}(k) - i_{ref,ix}(k) \tag{3}$$

where $i_{S,ix}(k)$ is the digital time-varying supply current signal; x refers to phase a or c. Furthermore, by referring to Equation (2), the reference current of the proposed CCA can be expressed as:

$$i_{ref,ix}(k) = i_{Fund,ext,ix}(k) + i_{dc,est}(k) \tag{4}$$

where $i_{Fund,ext,ix}(k)$ is the digital time-varying extracted fundamental load current signal.

As explained in the previous subtopic, the amplitudes of both $i_{Fund,ext,ix}(k)$ and $i_{dc,est}(k)$ signals are generated by the ADALINEs based fundamental component extraction algorithm [29] and the Crisp-PI self-charging dc-link VCA [30], respectively.

3.1. Proposed Adaptive Hybrid Fuzzy-Proportional Plus Crisp-Integral Current Controllers

Each proposed hybrid controller is developed by integrating Fuzzy-P and Crisp-I current controllers. The Fuzzy-P current controller is used to perform the proportional control action, by adaptively tuning the values of both the current proportional gain K_{pc} and the current integral gain K_{ic}. Whilst, the Crisp-I current controller is employed to perform the integral control action, and to enhance the steady-state control mechanism. A block diagram of the proposed hybrid controller is depicted in Figure 3.

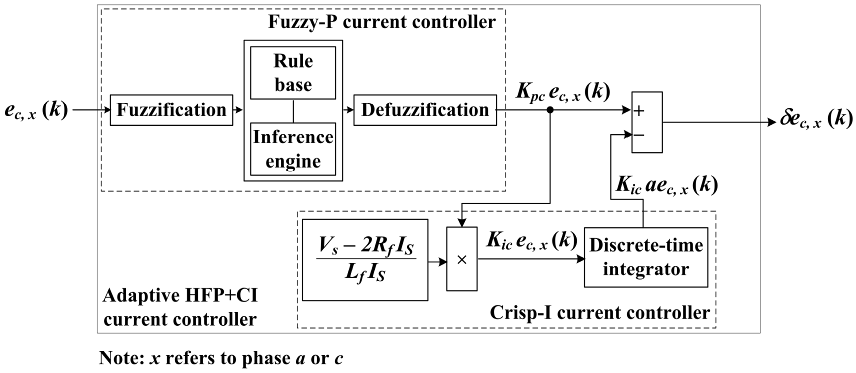

Figure 3. Block diagram of the proposed hybrid controller.

Firstly, the Fuzzy-P current controller is used to minimize $e_{c,ix}(k)$, by adaptively tuning the K_{pc} value. According to Figure 3, the operation of the controller starts with the evaluation and conversion of numerical $e_{c,ix}(k)$ input variable to membership grades of defined membership functions (MFs). This process is called fuzzification. Then, rule base and inference engine are used to evaluate and generate an aggregation of the fuzzified digital time-varying current proportional output variable $K_{pc}e_{c,ix}(k)$; it is based on a set of fuzzy rules. Lastly, the resulted $K_{pc}e_{c,ix}(k)$ set is converted to numerical $K_{pc}e_{c,ix}(k)$, during defuzzification process.

In this work, seven symmetrical triangular MFs for both input and output variables are employed. They are selected since they are simple to be built and computed [31], easy to be executed in both simulation and experimental work [31], and inherit low computational cost [25]. The normalized MF set is shown in Figure 4. All acronyms are defined as Negative Big (NB), Negative Medium (NM), Negative Small (NS), Zero (ZE), Positive Small (PS), Positive Medium (PM), and Positive Big (PB).

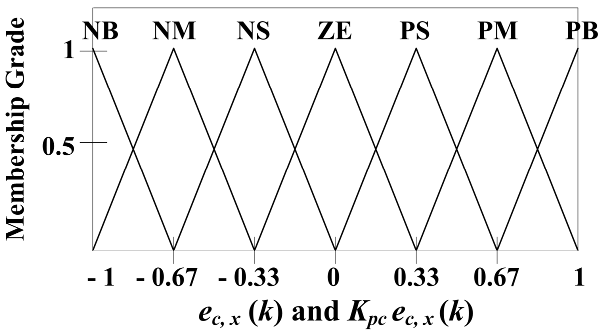

Figure 4. Normalized Membership Function set for $e_{c,ix}(k)$ and $K_{pc}e_{c,ix}(k)$.

The boundary of the MF set is determined as follows:

1. For the MF set of $e_{c,ix}(k)$:

   The boundary is determined based on the response of the proposed CCA during the open-loop operation.

2. For the MF set of $K_{pc}e_{c,ix}(k)$:

   The boundary is determined based on the total harmonic distortion (THD) value of $i_{S,ix}(t)$. At this moment, the SAPF applies a fixed V_{dc} supply; for eliminating the effect of the operation of the dc-link VCA. Thus, Equation (1) becomes:

$$i_{S,ix}(t) = i_{L,ix}(t) - i_{F,ix}(t) \tag{5}$$

Then, the rule base implements SISO fuzzy rules; for simplifying the controller structure. It is developed based on the relationship between $i_{S,ix}(k)$ and $i_{ref,ix}(k)$, and the relationship between $i_{S,ix}(t)$ and $i_{F,ix}(t)$. Both relationships can be expressed as in Equations (3) and (5); they can easily be interpreted in linguistic reasoning. Since the shape of $i_{L,ix}(t)$ remains unchanged throughout the compensation process, therefore the rule base is developed as follows:

1. If $e_{c,ix}(k)$ is positive:

   $i_{S,ix}(k)$ is higher than $i_{ref,ix}(k)$. Then, $i_{S,ix}(t)$ is reduced by increasing $i_{F,ix}(t)$. Hence, $K_{pc}e_{c,ix}(k)$is positive.

2. If $e_{c,ix}(k)$ is negative:

   $i_{S,ix}(k)$ is lower than $i_{ref,ix}(k)$. Then, $i_{S,ix}(t)$ is increased by decreasing $i_{F,ix}(t)$. Hence, $K_{pc}e_{c,ix}(k)$ is negative.

All fuzzy rules are tabulated in Table 1.

Table 1. Fuzzy rules of the Fuzzy-P current controller.

$e_{c,ix}(k)$	$K_{pc}e_{c,ix}(k)$
NB	NB
NM	NM
NS	NS
ZE	ZE
PS	PS
PM	PM
PB	PB

Regarding to the table, the Fuzzy-P current controller only requires to execute seven fuzzy rules, which is a square root of the fuzzy rules of the Fuzzy-PI current controller in [28]. In this work, the controller applies the Mamdani "min" inference engine. It is chosen due to its simple and easy implementation. Furthermore, the principle operation of the inference engine is motivated by intuitive clarity [32].

Next, the defuzzification process is conducted using the centroid technique. The centre of gravity (COG) of resulted $K_{pc}e_{c,ix}(k)$ set is calculated using this following equation:

$$\text{COG} = \frac{\sum_i \mu\left(K_{pc}e_{c,ix}(k)_i\right) K_{pc}e_{c,ix}(k)_i}{\sum_i \mu\left(K_{pc}e_{c,ix}(k)_i\right)} \tag{6}$$

where $\mu\left(K_{pc}e_{c,ix}(k)_i\right)$ is the membership degree of resulted $K_{pc}e_{c,ix}(k)$ set, and $K_{pc}e_{c,ix}(k)_i$ is the point of resulted $K_{pc}e_{c,ix}(k)$ set. The COG value represents numerical $K_{pc}e_{c,ix}(k)$.

Subsequently, the output variable $K_{pc}e_{c,ix}(k)$ of the Fuzzy-P current controller is further be utilized; to modify and control the K_{ic} value of the Crisp-I current controller for eliminating $e_{c,ix}(k)$. It will be implemented in a simple Crisp-PI tuning algorithm of controlling the operation of SAPFs [33]:

$$K_{ic} = K_{pc}\left(\frac{V_{s,ix} - 2I_{S,ix}R}{I_{S,ix}L}\right) \tag{7}$$

where $V_{S,ix}$ it the peak amplitude of $v_{S,ix}(t)$, $I_{S,ix}$ it the peak amplitude of $i_{S,ix}(t)$, and R and L are the resistance and inductance of the filter inductor L_f. In regard to the structure of the proposed hybrid controller, Equation (7) can be written as:

$$K_{ic}e_{c,ix}\left(k\right) = K_{pc}e_{c,ix}\left(k\right)\left(\frac{V_{s,ix} - 2I_{S,ix}R}{I_{S,ix}L}\right) \quad (8)$$

Based on Figure 3, the integration of $K_{ic}e_{c,ix}\left(k\right)$ produces the digital time-varying current integral output variable $K_{ic}ae_{c,ix}\left(k\right)$. Later, the digital time-varying current control signal $\delta e_{c,ix}\left(k\right)$ is generated using this following equation:

$$\begin{aligned} \delta e_{c,ix}\left(k\right) &= K_{pc}e_{c,ix}\left(k\right) + K_{ic}ae_{c,ix}\left(k\right) \\ &= K_{pc}e_{c,ix}\left(k\right) + \int_{t_{k-1}}^{t_k} K_{ic}ae_{c,ix}\left(k\right)dk; k = 1,2,3,\ \ldots, n \\ &= K_{pc}e_{c,ix}\left(k\right) + \int_{t_{k-1}}^{t_k}\left(\frac{V_{s,ix}-2I_{S,ix}R}{I_{S,ix}L}\right)K_{pc}e_{c,ix}\left(k\right)dk \\ &= \frac{\sum_i \mu\left(K_{pc}e_{c,ix}(k)_i\right)K_{pc}e_{c,ix}(k)_i}{\sum_i \mu\left(K_{pc}e_{c,ix}(k)_i\right)} + \frac{V_{s,ix}-2I_{S,ix}R}{I_{S,ix}L}\int_{t_{k-1}}^{t_k}\frac{\sum_i \mu\left(K_{pc}e_{c,ix}(k)_i\right)K_{pc}e_{c,ix}(k)_i}{\sum_i \mu\left(K_{pc}e_{c,ix}(k)_i\right)}dk \end{aligned} \quad (9)$$

where t_k is the sampling time of sample data k, and n is the maximum number of sample data. According to Equation (9), it can be stated that both the K_{pc} and K_{ic} values are adaptively tuned, throughout the operation of the SAPF. Both gain values are tuned at each sample period.

3.2. Pulse Width Modulation Generator

Eventually, based on Figure 2, a 3-phase PWM switching signal is generated by comparing the 3-phase digital time-varying current control signal $\delta e_{c,iy}\left(k\right)$ with a digital up-down triangular carrier signal. Note that y refers to phase a, b or c. Since the proposed CCA only consists of two current controllers, hence, the control signal for phase b is produced using this following equation:

$$\delta e_{c,ib}\left(k\right) = -\delta e_{c,ia}\left(k\right) - \delta e_{c,ic}\left(k\right) \quad (10)$$

Thus, $\delta e_{c,ib}\left(k\right)$ is known as the dependent control signal.

In a 3-phase 3-wire VSI based SAPF operation, switching signals for both upper and lower switches of the filter must opposite to each other. Thus, the switching signal for the upper switches is generated as follows:

1. If $\delta e_{c,iy}\left(k\right)$ is greater than the carrier signal, then the switching signal equals to 1.
2. If $\delta e_{c,iy}\left(k\right)$ is lower than the carrier signal, then the switching signal equals to 0.

Additionally, the digital carrier signal is generated using a counter mode and it can be calculated as:

$$\text{Counter} = \frac{\text{sampling frequency (Hz)}}{2 \times \text{switching frequency (Hz)}} \quad (11)$$

In this work, the sampling frequency is set at 150 kHz and the switching frequency is 25 kHz. The switching frequency is not considered high and it will not lead to electromagnetic interference (EMI) problem; the conducted EMI is commonly measured within the range of 150 kHz to 30 MHz [34].

4. Simulation Work

Table 2 tabulates all parameters adopted in the simulation work. According to Figure 2, the SAPF operates with two different types of NLs. There are capacitive NL (Load 1) and inductive NL (Load 2). In this work, the SAPF with the proposed CCA are constructed and simulated in MATLAB/Simulink.

This work is divided into four parts: the selection of the range of $K_{pc}e_c\left(k\right)$'s MF set boundary, the verification of the effectiveness of the proposed CCA, the comparison of the performance of the proposed CCA with other PI-type CCAs, and the study of the effect of using different CCAs on V_{dc} regulation.

Table 2. Specification adopted in both simulation and experimental work.

Description		Value
3-phase line-to-line voltage supply		100 V
Line inductor L_s		5 mH
Filter inductor L_f		5 mH
Dc-link capacitor C_{dc}		2200 µF
Dc-link voltage reference $V_{dc,ref}$		300 V
Load 1:	Resistor R_1	43 Ω and 63 Ω
	Capacitor C_1	470 µF
Load 2:	Resistor R_2	43 Ω and 63 Ω
	Inductor L_1	80 mH

4.1. Selection of the Range of $K_{pc}e_c$ (k)'s Membership Function Set Boundary

In this procedure, the SAPF is connected to a fixed 300 V dc voltage supply. The selection of the boundary depends on the THD value of $i_{S,a}$ (t), using Load 1 and Load 2. Therefore, the boundary is varied until THD value of $i_{S,a}$ (t) below than 5%.

Theoretically, since the Fuzzy-P current controller in the proposed CCA adopts a proportional (P) control mechanism, thus, the higher $K_{pc}e_c$ (k)'s MF set boundary will supposedly result lower THD value. Nevertheless, as similar as P controllers, too high $K_{pc}e_c$ (k)'s MF set boundary leads to unstable control system. Hence, increasing the THD value of $i_{S,a}$ (t). A graph of THD values corresponding to variable $K_{pc}e_c$ (k)'s MF set boundaries is shown in Figure 5.

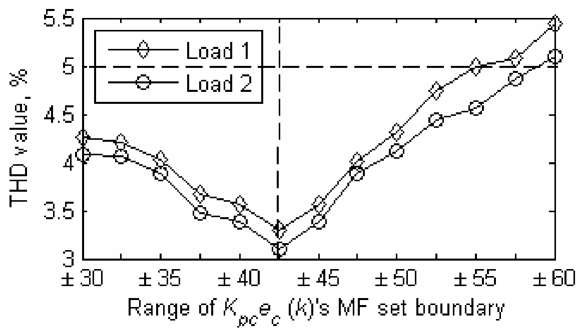

Figure 5. Relationship between variable $K_{pc}e_c$ (k)'s Membership Function set boundary and THD value.

Based on the figure, it can be observed that the $K_{pc}e_c$ (k)'s MF set boundary between ±30 to ±55 has resulted THD value below 5%, for both Load 1 and Load 2. Hence, it can be stated that the value within the specified range is suitable to be used for achieving stable control system and low THD value. However, in order to obtain the lowest THD value for both Load 1 and Load 2, the most suitable value of $K_{pc}e_c$ (k)'s MF set boundary is ±42.5. On the other hand, the maximum $K_{pc}e_c$ (k)'s MF set boundary is ±55.

4.2. Harmonic Currents and Reactive Power Compensation

The fixed dc voltage supply in the previous procedure is replaced by a 2200 µF C_{dc}. Then, the effectiveness of the proposed CCA, in helping the SAPF to regulate i_S (t) and perform harmonic currents and reactive power compensation is verified. It is based on the waveshape, phase, THDs and PFs of 3-phase i_S (t).

This study is conducted during both steady-state and dynamic-state operations. Note that the dynamic-state operation refers to a condition in which Load 1 is instantaneously switched to Load 2. The switching happens at the switching-point equals to 3 seconds (s). Simulation waveforms of the measured $v_{S,ia}$ (t), $i_{L,ia}$ (t), $i_{F,ia}$ (t), $i_{ref,ia}$ (t), and 3-phase i_S (t)during steady-state and dynamic-state operations are depicted in Figures 6 and 7, respectively.

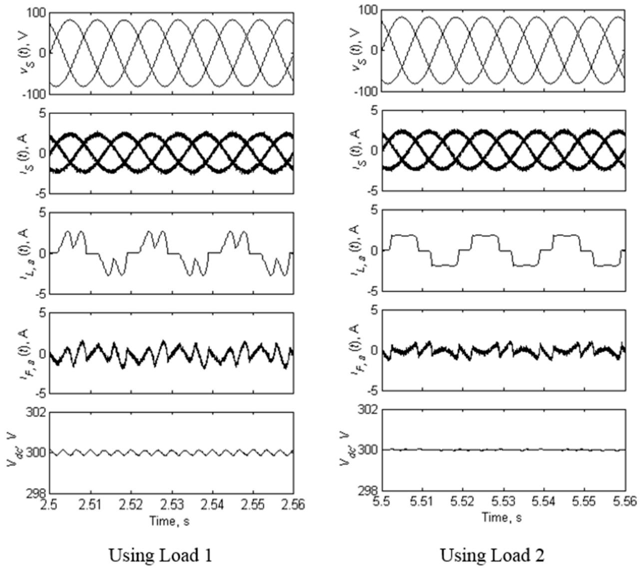

Figure 6. Simulated steady-state 3-phase $v_S(t)$ and $i_S(t)$, per-phase $i_{L,ia}(t)$ and $i_{F,ia}(t)$, and V_{dc} waveforms using Load 1 and Load 2. The SAPF applies the proposed CCA.

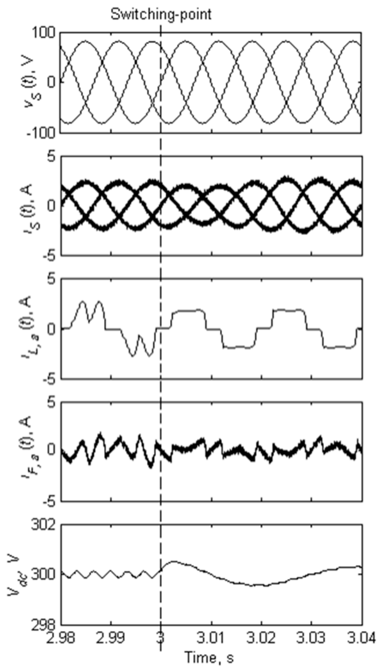

Figure 7. Simulated dynamic-state 3-phase $v_S(t)$ and $i_S(t)$, per-phase $i_{L,ia}(t)$ and $i_{F,ia}(t)$, and V_{dc} waveforms during the switching between Load 1 and Load 2. The SAPF applies the proposed CCA.

Based on the figures, it can be observed that the SAPF using the proposed CCA is capable to regulate $i_S(t)$ and perform harmonic currents compensation during both steady-state and dynamic-state operations. It is because the wave shapes of the measured 3-phase $i_S(t)$ are approximately sinusoidal and in phase with the measured $v_S(t)$. Furthermore, as shown in Figure 7, it can be seen that the proposed CCA is still capable to maintain the sinusoidal shape of the measured $i_S(t)$ right after the switching-point. All THD values of steady-state simulated 3-phase $i_S(t)$ for Load 1 and Load 2 are shown in Figure 8. The THD values are measured using the FFT analysis in MATLAB/ Simulink. The values are measured for 10 cycles of $i_S(t)$ with maximum harmonic order of

50 (1250 Hz). Before the SAPF implementation, THD values of the measured 3-phase $i_S\ (t)$ are 45.97% for Load 1 and 26.31% for Load 2.

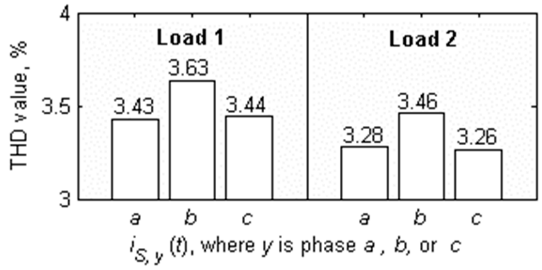

Figure 8. THD values of steady-state simulated 3-phase $i_S\ (t)$ using Load 1 and Load 2. The SAPF applies the proposed CCA.

Regarding the figure, it can be seen that the THD values (using Load 1 and Load 2) after the SAPF implementation have been reduced below 5%. Hence, the IEEE standard 519-2014 is met. Nevertheless, it can be observed that the THD value of $i_{S,\ ib}\ (t)$ is approximately 0.2% higher than the THD value of $i_{S,ia}\ (t)$ and $i_{S,ic}\ (t)$. It happens due to the execution of the dependent current control signal. Since the difference is very small, therefore it can be stated that this condition will not lowering the performance of the SAPF.

Other than harmonic currents compensation, Figure 9 presents reactive power waveforms consumed or generated by the NLs, main voltage supply and SAPF respectively; to verify the SAPF capability in compensating reactive power. The figure shows two sets of reactive power waveforms before and after the SAPF implementation.

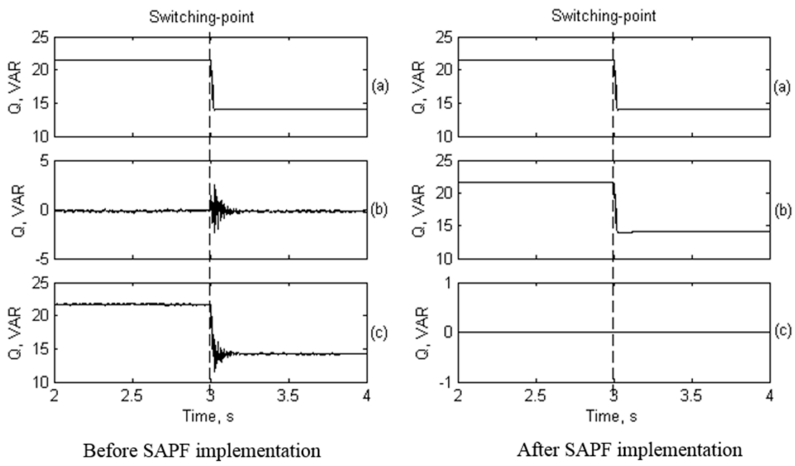

Figure 9. Reactive power consumed or generated by (**a**) both NLs, (**b**) main voltage supply and (**c**) SAPF during steady-state and dynamic-state operations.

Before the SAPF implementation, it can be seen in the figure that reactive power consumed by both NLs is supplied by the main voltage supply. Hence, PF of the system with either Load 1 or Load 2 has reduced from unity to 0.90 or 0.94. Nevertheless, by applying the SAPF, it can be observed that the reactive power supplied by the main voltage supply can be compensated. Thus, PF of the system has been corrected to 0.99 which is nearly unity PF.

4.3. Comparison of Performance with Other Proportional-Integral Current Control Algorithms

The performance of the proposed CCA is compared to the performance of Fuzzy-PI CCA and Crisp-PI CCA. The difference relies on the implementation of different current controllers. In this procedure, the dc-link VCA remains unchanged.

Block diagrams of both Fuzzy-PI and Crisp-PI current controllers are shown in Figure 10a,b, respectively. The Fuzzy-PI current controller implements symmetrical triangular MFs, 49 Fuzzy rules, the Mamdani inference engine, and the centroid technique. Meanwhile, K_p and K_i values of the Crisp-PI controller are tuned using a Crisp-PI tuning algorithm presented in [33]; they are 14.67 and 97213.2, respectively.

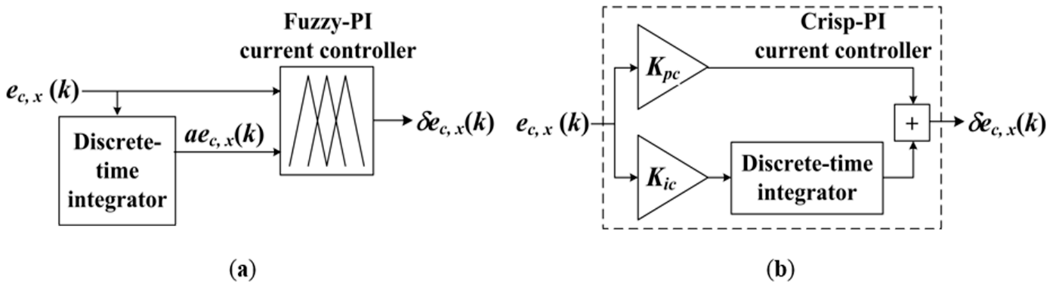

Figure 10. Block diagrams of (**a**) Fuzzy-PI and (**b**) Crisp-PI current controllers.

Figures 11 and 12 present simulated steady-state and dynamic-state 3-phase $v_S(t)$, 2 phases $i_{ref,ix}(k)$, and 3-phase $i_S(t)$ waveforms using different PI-type CCAs, respectively. Additionally, THD values of simulated steady-state 3-phase $i_S(t)$ are presented in Figure 13.

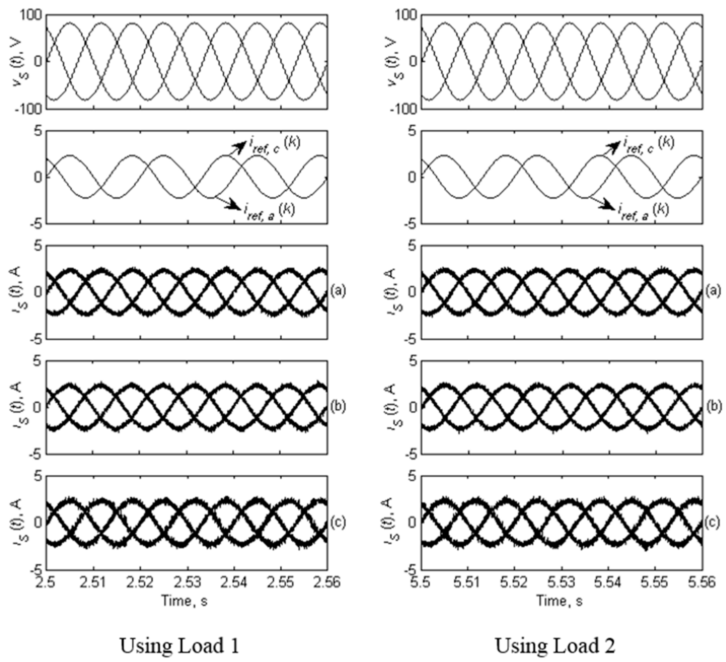

Figure 11. Simulated steady-state 3-phase $v_S(t)$, 2 phases $i_{ref,ix}(k)$, and 3-phase $i_S(t)$ waveforms using Load 1 and Load 2. The SAPF applies the (**a**) proposed, (**b**) Fuzzy-PI or (**c**) Crisp-PI CCA.

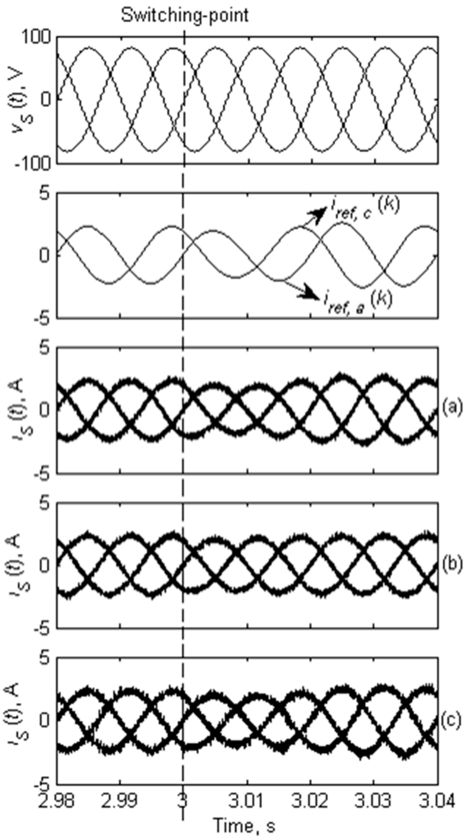

Figure 12. Simulated dynamic-state 3-phase $v_S(t)$, 2 phases $i_{ref,ix}(k)$, and 3-phase $i_S(t)$ waveforms during the switching between Load 1 and Load 2. The SAPF applies the (**a**) proposed, (**b**) Fuzzy-PI or (**c**) Crisp-PI CCA.

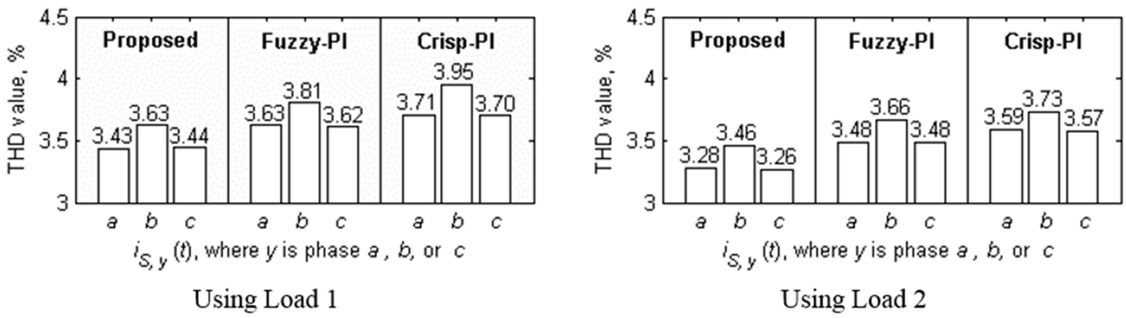

Figure 13. THD values of simulated steady-state 3-phase $i_S(t)$ using Load 1 and Load 2. The SAPF applies the (a) Proposed, (b) Fuzzy-PI or (c) Crisp-PI CCA.

During the steady-state operation, it can be seen that the measured 3-phase $i_S(t)$ waveform using the proposed CCA as shown in Figure 11a is similar as the measured 3-phase $i_S(t)$ waveform using the Fuzzy-PI CCA as shown in Figure 11b. Hence, it can be stated that the proposed CCA inherits the same control behaviour as the Fuzzy-PI CCA. However, according to Figure 13, it can be observed that the implementation of the proposed CCA has resulted lower THD values than using the Fuzzy-PI CCA. In addition, as compared to the measured 3-phase $i_S(t)$ waveform using the PI CCA (in Figure 11c), it can be confirmed that the implementation of the proposed CCA is capable to reduce ripple current produced by the execution of the Crisp-PI CCA. In this procedure, all PFs using both CCAs have been corrected to nearly unity. On the other hand, during dynamic-state operation, it can be observed in Figure 12 that the response of all PI-types CCAs is similar.

In overall, it can be confirmed that the implementation of the proposed CCA can reduce ripple current and THD values of 3-phase $i_S(t)$. According to Figure 13, the resulted THD values using of the proposed CCA is 6% lower than using the Fuzzy-PI CCA, and 8% lower than using the PI CCA.

Eventually, real power consumed by the SAPF is measured. Note in Figure 1 that the direction $i_F(t)$ is opposite to the direction of $i_S(t)$. Thus, a negative sign of power indicates that the SAPF consumes the real power. Figure 14 presents real power consumed by the SAPF.

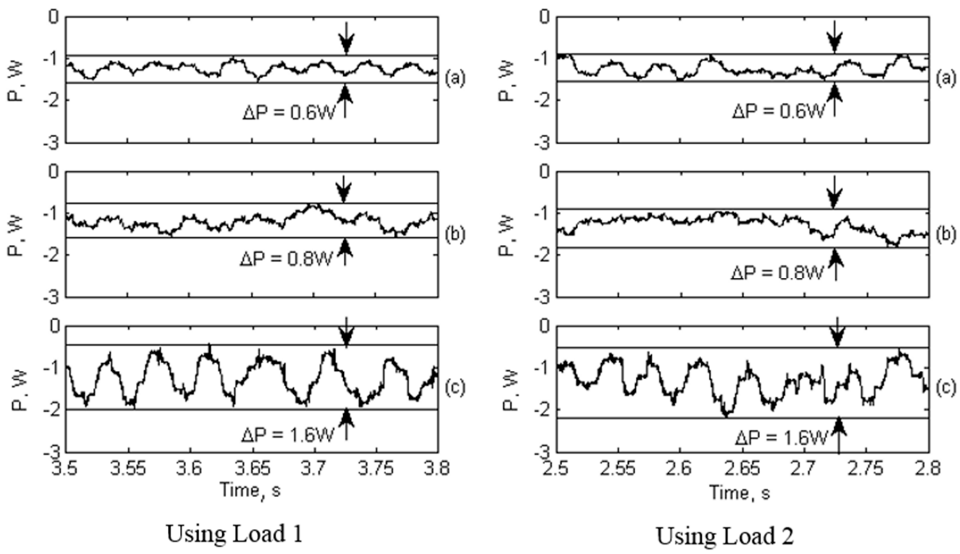

Figure 14. Real power consumed by the SAPF using Load 1 and Load 2. The SAPF applies the (**a**) Proposed, (**b**) Fuzzy-PI or (**c**) Crisp-PI CCA.

According to the figure, it can be observed that value of real power consumed by the SAPF is fluctuated within different power ranges. As mentioned, the SAPF requires real power for regulating its V_{dc} value, and compensating its power loss. Since the SAPF only utilizes the Crisp-PI VCA, therefore, it can be claimed that the required real power for V_{dc} regulation is fixed, regardless of PI-type CCAs. According to the maximum real power (negative sign is neglected), the SAPF using Load 1 and the proposed CCA in Figure 14a has consumed 14.8% and 28.1% lower real power than using the Fuzzy-PI CCA in Figure 14b and the Crisp-PI CCA in Figure 14c respectively. Meanwhile, the SAPF using Load 2 and the proposed or Fuzzy-PI CCA has consumed same real power. Nevertheless, the power is 21% lower than using the Crisp-PI CCA. In overall, it can be stated that the SAPF using the proposed CCA has consumed lower real power than using the Fuzzy-PI CCA and Crisp-PI CCA. Consequently, it can be confirmed that the use of the proposed CCA is capable of reducing power losses in the SAPF. Additionally, it can be seen in the figure that the implementation of the proposed CCA is also capable to reduce real power fluctuation; it is 25% lower than using the Fuzzy-PI CCA and 62.5% lower than using the Crisp-PI CCA.

5. Experimental Work

Since the implementation of the proposed CCA exhibits better outcome than the other PI-type CCAs, therefore this work only focuses on validating the performance of the proposed CCA, during steady-state and dynamic-state operations of the SAPF. A hardware prototype of the SAPF is constructed using all specifications tabulated in Table 2. The experimental setup is shown in Figure 15. Then, the proposed CCA is built and executed in DSP TMS320F28335. Also, code composer studio (CCS) v3.3 is employed to write and compile the algorithm in C language.

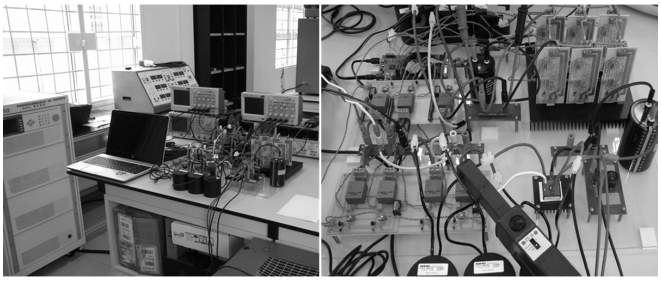

Figure 15. Experimental setup.

Experimental steady-state waveforms of $v_{S,ia}(t)$, 3-phase $i_S(t)$, $i_{L,ia}(t)$, and $i_{F,ia}(t)$ using Load 1 and Load 2 are presented in Figures 16 and 17, respectively. According to both figures, it can be noticed that the measured $i_{S,ia}(t)$ waveform is in sinusoidal shape and in phase with the measured $v_{S,ia}(t)$. Furthermore, the measured 3-phase $i_S(t)$ waveforms also inherit sinusoidal shape. Based on these results, it can be validated that the SAPF using the proposed CCA is capable to regulate $i_S(t)$ and compensate harmonic currents and reactive power.

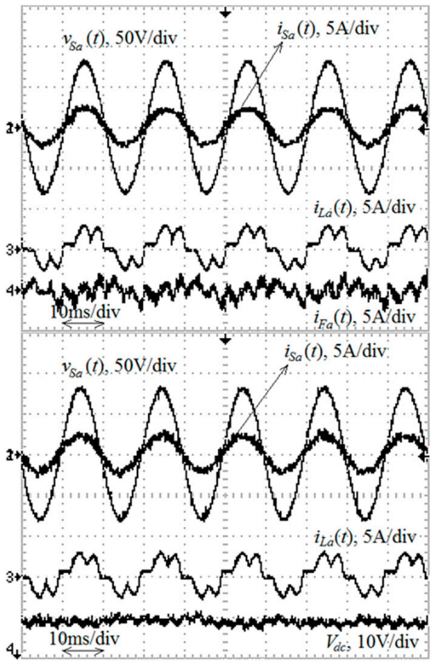

(a)

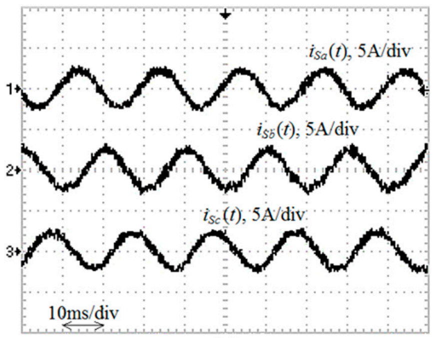

(b)

Figure 16. Experimental steady-state (**a**) $v_{S,a}(t)$, $i_{S,ia}(t)$, $i_{L,ia}(t)$, $i_{F,ia}(t)$, V_{dc} and (**b**) 3-phase $i_S(t)$ waveforms, using Load 1.

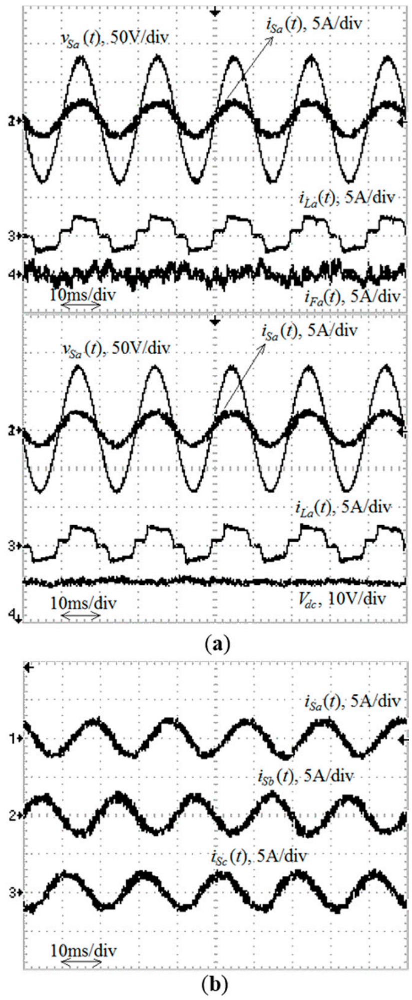

Figure 17. Experimental steady-state (**a**) $v_{S,a}\,(t)$, $i_{S,ia}\,(t)$, $i_{L,ia}\,(t)$, $i_{F,ia}\,(t)$, V_{dc} and (**b**) 3-phase $i_S\,(t)$ waveforms, using Load 2.

Next, THD values of steady-state 3-phase $i_S\,(t)$ after the implantation of the SAPF are presented in Figure 18. By using information from oscilloscope's data loggers, the THD value is calculated using the FFT analysis in MATLAB/ Simulink. The values are measured for 10 cycles of $i_S\,(t)$ with maximum harmonic order of 50 (1250 Hz). Before the SAPF implementation, THD values of the measured 3-phase $i_S\,(t)$ are 33.6% for Load 1 and 24.6% for Load 2. Based on the figure, it can be observed that the THD values have successfully reduced below 5%. Hence, the IEEE standard 519-2014 is complied. Also, all measured PFs of steady-state 3-phase $i_S\,(t)$ have been corrected from 0.90 for Load 1 and 0.94 for Load 2 to nearly unity (0.99) PF.

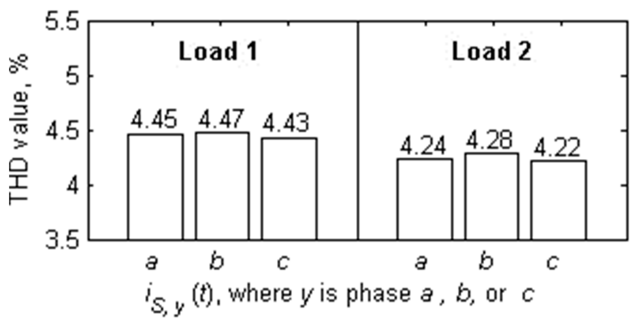

Figure 18. THD values of steady-state 3-phase $i_S\,(t)$ after the SAPF implementation.

Then, this study is continued with performance validation of the proposed CCA during the dynamic-state operation. Figure 19 shows $v_{S,ia}(t)$, $i_{S,ia}(t)$, $i_{L,ia}(t)$, and $i_{F,\ ia}(t)$ waveforms during this operating condition.

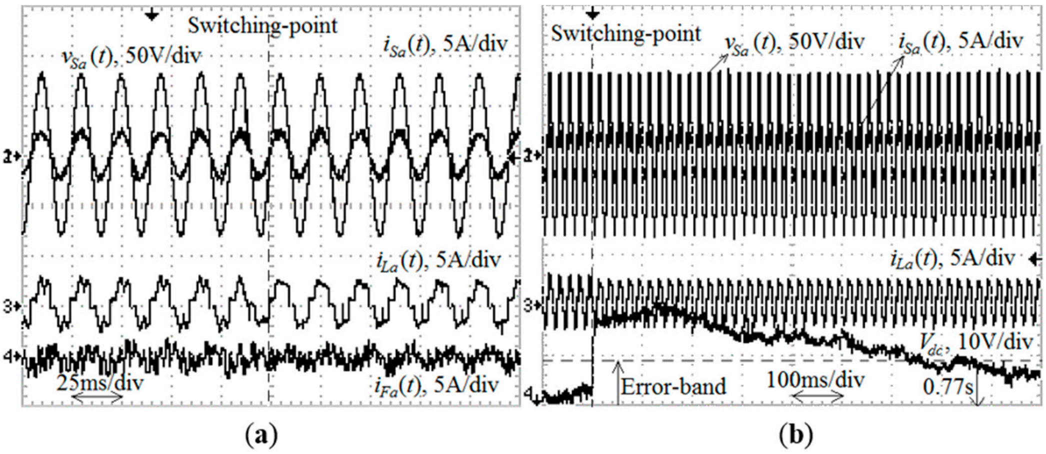

Figure 19. Experimental dynamic-state (**a**) $v_{S,ia}(t)$,$i_{S,ia}(t)$, $i_{L,ia}(t)$, $i_{F,ia}(t)$, and (**b**) 3-phase $i_S(t)$ waveforms during the switching between Load 1 and Load 2.

Based on the figure, it can be seen that the SAPF using the proposed CCA is still capable to compensate harmonic currents, right after the switching-point. Thus, the shape and the phase of the measured $i_{S,ia}(t)$ remain unchanged. According to all experimental results, it can be confirmed that the proposed CCA can be utilized to regulate $i_S(t)$ during steady-state and dynamic-state operation. Eventually, the SAPF is capable to compensate both harmonic currents and reactive power effectively.

6. Conclusions

The proposed adaptive HFP+CI CCA is successfully developed and executed. Hence, the SAPF is capable of controlling $i_S(t)$ and perform harmonic currents and reactive power compensation effectively. In this work, all results of using the proposed CCA in both simulation and experimental work have shown good agreement. The results have validated that the implementation of the integration of the Fuzzy-P current controller (with simple structure and less fuzzy rules) and the Crisp-I current controller does improve the steady-state control mechanism of the proposed CCA. Therefore, the use of the proposed CCA has resulted lower THD values than using the Fuzzy-PI CCA and Crisp-PI CCA. Additionally, it can be stated that implementation of the proposed CCA can enhance the SAPF operation.

Acknowledgments: This work is supported by the High Performance Individual – Universiti Putra Malaysia Grant under GP-IBT/2013/9417200.

Author Contributions: Nor Farahaida Abdul Rahman developed the main parts of the research work. It includes the simulation model, hardware set up, and analyses of simulation and hardware results. She was mainly responsible for preparing the paper. Mohd Amran Mohd Radzi contributed in experimental and writing parts. Azura Che Soh, Norman Mariun and Nasrudin Abd Rahim also involved in verifying the work and actively contributed to finalize the manuscript.

Conflicts of Interest: The authors declare no conflict of interest.

References

1. Rashid, M.H. *Power Electronics Handbook Devices, Circuits, and Applications*, 3rd ed.; Elsevier: Oxford, UK, 2011; pp. 1–1193.
2. Shahbaz, M. Active Harmonics Filtering for Distributed AC Systems. Master's Thesis, Norwegian University of Science and Technology, Trondheim, Norway, 2012.

3. Singh, B.; Al-Haddad, K.; Chandra, A. A review of active filters for power quality improvement. *IEEE Trans. Ind. Electron.* **1999**, *46*, 960–971. [CrossRef]
4. Bouloumpasis, I.; Vovos, P.; Georgakas, K.; Vovos, N. Current harmonics compensation in microgrids exploiting the power electronics interfaces of renewable energy sources. *Energies* **2015**, *8*, 2295–2311. [CrossRef]
5. Qasim, M.; Kanjiya, P.; Khadkikar, V. Artificial-neural-network-based phase-locking scheme for active power filters. *IEEE Trans. Ind. Electron.* **2014**, *61*, 3857–3866. [CrossRef]
6. Kinhal, V.G.; Agarwal, P.; Gupta, H.O. Performance investigation of neural-network-based unified power-quality conditioner. *IEEE Trans. Power Deliv.* **2011**, *26*, 431–437. [CrossRef]
7. Singh, B.; Verma, V.; Solanki, J. Neural network-based selective compensation of current quality problems in distribution system. *IEEE Trans. Ind. Electron.* **2007**, *54*, 53–60. [CrossRef]
8. Bojoi, R.; Limongi, L.R.; Roiu, D.; Tenconi, A. Enhanced power quality control strategy for single-phase inverters in distributed generation systems. *IEEE Trans. Power Electron.* **2011**, *26*, 798–806. [CrossRef]
9. Xin, T.; Tsang, K.M.; Chan, W.L. A power quality compensator with dg interface capability using repetitive control. *IEEE Trans. Energy Convers.* **2012**, *27*, 213–219.
10. Ramos, G.A.; Costa-Castelló, R. Power factor correction and harmonic compensation using second-order odd-harmonic repetitive control. *IET Control Theory Appl.* **2012**, *6*, 1633–1644. [CrossRef]
11. Hamad, M.S.; Masoud, M.I.; Williams, B.W.; Finney, S. Medium voltage 12-pulse converter: AC side compensation using a shunt active power filter in a novel front end transformer configuration. *IET Power Electron.* **2012**, *5*, 1315–1323. [CrossRef]
12. Yaramasu, V.; Rivera, M.; Bin, W.; Rodriguez, J. Model Predictive Current Control of Two-Level Four-Leg Inverters-Part I: Concept, Algorithm, and Simulation Analysis. *IEEE Trans. Power Electron.* **2013**, *28*, 3459–3468. [CrossRef]
13. Rivera, M.; Yaramasu, V.; Rodriguez, J.; Bin, W. Model predictive current control of two-level four-leg inverters-part ii: Experimental implementation and validation. *IEEE Trans. Power Electron.* **2013**, *28*, 3469–3478. [CrossRef]
14. Matas, J.; de Vicuna, L.G.; Miret, J.; Guerrero, J.M.; Castilla, M. Feedback linearization of a single-phase active power filter via sliding mode control. *IEEE Trans. Power Electron.* **2008**, *23*, 116–125. [CrossRef]
15. Djazia, K.; Krim, F.; Chaoui, A.; Sarra, M. Active power filtering using the ZDPC method under unbalanced and distorted grid voltage conditions. *Energies* **2015**, *8*, 1584–1605. [CrossRef]
16. Chandra, A.; Singh, B.; Singh, B.N.; Al-Haddad, K. An improved control algorithm of shunt active filter for voltage regulation, harmonic elimination, power-factor correction, and balancing of nonlinear loads. *IEEE Trans. Power Electron.* **2000**, *15*, 495–507. [CrossRef]
17. Rahmani, S.; Hamadi, A.; Al-Haddad, K.; Dessaint, L.A. A combination of shunt hybrid power filter and thyristor-controlled reactor for power quality. *IEEE Trans. Ind. Electron.* **2014**, *61*, 2152–2164. [CrossRef]
18. Rahmani, B.; Li, W.; Liu, G. A wavelet-based unified power quality conditioner to eliminate wind turbine non-ideality consequences on grid-connected photovoltaic systems. *Energies* **2016**, *9*, 390. [CrossRef]
19. Panda, A.K.; Mikkili, S. FLC based shunt active filter (p-q and i_d-i_q) control strategies for mitigation of harmonics with different fuzzy mfs using matlab and real-time digital simulator. *Int. J. Electr. Power Energy Syst.* **2013**, *47*, 313–336. [CrossRef]
20. Chang, G.W.; Shee, T.C. A novel reference compensation current strategy for shunt active power filter control. *IEEE Trans. Power Deliv.* **2004**, *19*, 1751–1758. [CrossRef]
21. Vodyakho, O.; Mi, C.C. Three-Level inverter-based shunt active power filter in three-phase three-wire and four-wire systems. *IEEE Trans. Power Electron.* **2009**, *24*, 1350–1363. [CrossRef]
22. Chen, Z.; Wang, Z.; Chen, M. Four hundred hertz shunt active power filter for aircraft power grids. *IET Power Electron.* **2014**, *7*, 316–324. [CrossRef]
23. Xiao, Z.; Deng, X.; Yuan, R.; Guo, P.; Chen, Q. Shunt active power filter with enhanced dynamic performance using novel control strategy. *IET Power Electron.* **2014**, *7*, 3169–3181. [CrossRef]
24. Odavic, M.; Biagini, V.; Zanchetta, P.; Sumner, M.; Degano, M. One-sample-period-ahead predictive current control for high-performance active shunt power filters. *IET Power Electron.* **2011**, *4*, 414–423. [CrossRef]
25. Kumar, P.; Mahajan, A. Soft computing techniques for the control of an active power filter. *IEEE Trans. Power Deliv.* **2009**, *24*, 452–461. [CrossRef]
26. Luo, A.; Shuai, Z.; Zhu, W.; Shen, Z.J. Combined system for harmonic suppression and reactive power compensation. *IEEE Trans. Ind. Electron.* **2009**, *56*, 418–428. [CrossRef]

27. Suetake, M.; da Silva, I.N.; Goedtel, A. Embedded DSP-based compact fuzzy system and its application for induction-motor v/f speed control. *IEEE Trans. Ind. Electron.* **2011**, *58*, 750–760. [CrossRef]
28. Kirawanich, P.; Oconnell, R.M. Fuzzy logic control of an active power line conditioner. *IEEE Trans. Power Electron.* **2004**, *19*, 1574–1585. [CrossRef]
29. Rahman, N.F.A.; Radzi, M.A.M.; Soh, A.C.; Mariun, N.; Rahim, N.A. Dual function of unified adaptive linear neurons based fundamental component extraction algorithm for shunt active power filter operation. *Int. Rev. Electr. Eng.* **2015**, *10*, 544–552.
30. Rahman, N.F.A.A.; Radzi, M.A.M.; Mariun, N.; Soh, A.C.; Rahim, N.A. Integration of dual intelligent algorithms in shunt active power filter. In Preceedings of the 2013 IEEE Conference on Clean Energy and Technology, Langkawi, Malaysia, 18–20 November 2013.
31. Suresh, Y.; Panda, A.K.; Suresh, M. Real-time implementation of adaptive fuzzy hysteresis-band current control technique for shunt active power filter. *IET Power Electron.* **2012**, *5*, 1188–1195. [CrossRef]
32. Jantzen, J. *Foundation of Fuzzy Control*, 1st ed.; Wiley: London, UK, 2007; pp. 1–57.
33. Bhattacharya, A.; Chakraborty, C. A shunt active power filter with enhanced performance using ann-based predictive and adaptive controllers. *IEEE Trans. Ind. Electron.* **2011**, *58*, 421–428. [CrossRef]
34. Borisov, K.; Ginn, H.L.; Trzynadlowski, A.M. Attenuation of electromagnetic interference in a shunt active power filter. *IEEE Trans. Power Electron.* **2007**, *22*, 1912–1918. [CrossRef]